AIAA JOURNAL
Vol. 32, No. 4, April 1994

Numerical Simulation of Shock-Box Interaction Using an Adaptive Finite Element Scheme

Joseph D. Baum*
Science Applications International Corporation, McLean, Virginia 22102
and
Rainald Löhner†
George Washington University, Washington, D.C. 20052

A transient, two-dimensional, finite element shock-capturing scheme on unstructured grids was applied to the study of a shock interacting with a box suspended above a rigid elevated surface. The area between the box and the surface was partially blocked by the box support beams, resulting in complex shock diffraction processes. The results demonstrate the capability of the developed adaptive refinement/coarsening algorithm to properly adapt to weak shocks, expansions, and contact discontinuities, and highlight the resulting excellent resolution of the captured flow features. In addition to interesting shock diffraction and propagation phenomena, the results demonstrate the capability of the new code to capture, and define in great detail, vortex sheets shed from sharp corners. We show that the baroclinic effect, an inviscid process, controls the shedding phenomenon during the diffraction phase. Hence, the Eulerian model is able to correctly predict this process.

Introduction

DURING the past ten years the computational fluid dynamics (CFD) community has experienced a proliferation of shock capturing schemes whose ultimate objective is the sharp, nonoscillatory capturing of transient shocks, including those that have propagated great distances.[1–3] The practical objective of these methodologies is to predict the loads exerted by shocks, initiated by nuclear or high-explosive bursts, on stationary or moving structures located a long distance from the burst point. The results of such simulations should help improve targeting specification requirements (for offensive purposes) or hardening criteria (for defensive objectives). From the point of view of numerical algorithm development, the long propagation times and distances that the shocks are likely to traverse from burst to impact point pose significantly greater demands than those required by traditional shock capturing schemes, which are only intended to produce steady, sharp, nonoscillatory shocks on airfoils, etc.[4–6] to yield the steady lift and drag forces. Past simulations of shock wave propagation over long distances relied on either a fixed-mesh structured grid approach[2] or sliding refined zones, intended to continuously surround the shocks with a finer mesh than elsewhere in the domain.[7] The first approach yielded coarser, diffused shocks after some propagation distance, since even for two-dimensional calculations it is not economically feasible, even with present-day class VI computers, to grid a domain of several hundreds or thousands of meters with 1-cm-size cells. The second approach was much more economical, as only part of the domain was finely refined. Nevertheless, the computational resources required for two-dimensional computations (both memory and computational time) were very high, while three-dimensional computations would have been prohibitively expensive for production-type runs. Hence, the objective of the present effort was a natural evolution of past deficiencies, i.e., to develop a numerical scheme capable of dynamically adapting to traveling shocks and other flow discontinuities. This approach allows us to use coarse grid resolution everywhere in the computational domain where flow gradients are low, while applying very fine grid resolution wherever better flow resolution is required. Hence, shocks should always advance into finely refined zones, while grid coarsening should be obtained in areas already traversed by the shocks.

The paper will first describe the CFD methodology employed, starting with the design criteria used for the flow solver. Thereafter, the adaptive refinement scheme employed is presented, followed by an extensive description of the results obtained for the shock-box case studied. The accent of the paper is on the results rather than on the algorithms employed. Therefore, the exposition of the algorithms is kept to a sufficient, but not exhaustive, depth.

CFD Methodology

The objective of the present effort was to develop efficient computational techniques for the simulation of strongly unsteady flows past bodies of complex geometrical shape. Therefore, the flow solver must be based on grid systems that can discretize domains of arbitrary complexity, be able to simulate moving or stationary shocks without spurious overshoots, and be able to allocate in the most efficient manner the degrees of freedom or equivalent computational resources during the course of a simulation. In the present case, these three design criteria are met as follows:

1) To discretize domains of arbitrary complexity, unstructured grids in conjunction with finite-element methods are used.

2) To accurately simulate the strong shocks present in the flowfields, a high-resolution, monotonicity-preserving algorithm for unstructured grids is used. The method, called FEM-FCT, is based on Zalesak's[8] generalization of the flux-corrected transport (FCT) algorithms of Boris and Book[9,10] to multidimensional problems.

3) To allocate in the most efficient manner the degrees of freedom of the mesh, an efficient adaptive refinement technique for transient problems is employed.

The Flow Solver: FEM-FCT

As stated above, high-resolution, monotonicity-preserving schemes must be developed to simulate the strong nonlinear discontinuities present in the flows under consideration. A number of these schemes have been developed over the last years.[4–6,11,12] The scheme used here is based on Zalesak's generalization[8] of the one-dimensional FCT schemes of Boris and Book.[9,10] Parrott and Christie[13] first analyzed FCT schemes in the context of finite element methods, and Löhner et al.[14,15] extended these ideas further to include the solution of systems of equations and the consistent-mass matrix that yields high temporal accuracy.

Received May 9, 1989; revision received Feb. 1, 1993; accepted for publication Feb. 1, 1993.

*Senior Research Scientist, Applied Physics Operations. Associate Fellow AIAA.
†Associate Research Professor, CMMEE, School of Engineering and Applied Science. Member AIAA.

Consider a set of conservation laws given by a system of partial differential equations of the form

$$\frac{\partial U}{\partial t} + \frac{\partial F_a^i}{\partial x^i} = \frac{\partial F_v^i}{\partial x^i} \tag{1}$$

where the advective fluxes $F_a = F_a(U)$ dominate the viscous fluxes $F_v = F_v(U)$. For flows described by Eq. (1), discontinuities in the variables may arise (e.g., shocks or contact discontinuities). Any numerical scheme of an order higher than unity will produce overshoots or ripples at such discontinuities (the so-called Godunov theorem). Very often, particularly for mildly nonlinear systems, these overshoots can be tolerated. However, for the class of problems studied here, overshoots will eventually lead to numerical instability, and will therefore have to be suppressed.

The FCT algorithm combines a high-order scheme with a low-order scheme in such a way that in regions where the variables under consideration vary smoothly (so that a Taylor expansion makes sense) the high-order scheme is used, whereas in those regions where the variables vary abruptly, the low-order scheme is favored.

The temporal discretization of Eq. (1) yields

$$U^{n+1} = U^n + \Delta U \tag{2}$$

where ΔU is the increment of the unknowns obtained for a given scheme at time $t = t^n$. Our aim is to obtain a ΔU of as high an order as possible without introducing overshoots. To this end, we rewrite Eq. (2) as

$$U^{n+1} = U^n + \Delta U^l + (\Delta U^h - \Delta U^l) \tag{3}$$

or

$$U^{n+1} = U^l + (\Delta U^h - \Delta U^l) \tag{4}$$

Here ΔU^h and ΔU^l denote the increments obtained by some high- or low-order scheme, whereas U^l is the (ripple-free) solution at time $t = t^{n+1}$ of the low-order scheme. The idea behind FCT is to limit the second term on the right side of Eq. (4):

$$U^{n+1} = U^l + \lim(\Delta U^h - \Delta U^l) \tag{5}$$

in such a way that no new overshoots or undershoots are created. In addition, strict conservation on the discrete level must be maintained. The simplest way to guarantee strict conservation for node-centered schemes (only these are considered here) is by constructing schemes for which the sum of the contributions of each individual element (cell) to its surrounding nodes vanishes (all that comes in goes out). This means that the limiting process [Eq. (5)] will have to be carried out in the elements (cells). Further details may be found in Refs. 14 and 15.

Transient Adaptive Refinement

A very attractive feature of schemes based on unstructured grids is the ease with which they incorporate adaptive refinement. The addition of further degrees of freedom does not destroy any previous structure. Thus, the flow solver requires no further modifications when operating on an adapted grid. For many practical problems, the regions that need to be refined are extremely small compared with the overall computational domain. Therefore, storage and CPU requirements are typically reduced by a factor of 10–100 when compared to an overall fine-resolution fixed mesh.[16–22] It has been our experience that, for production runs, adaptive refinement has been the crucial element necessary to perform simulations at an acceptable level of accuracy in a reasonable amount of time. The simulation presented in this paper is a typical example of such runs.

Several authors have studied these adaptive refinement schemes.[7,16,2–25] When developing an efficient adaptation methodology for transient problems, further constraints have to be considered. The method must be conservative, i.e., a mesh change should not result in the production or loss of mass, momentum, or energy, as this will produce erroneous shock propagation speed or will diffuse shocks or contact discontinuities. The method should not produce elements that are too small, as this will significantly reduce the allowable time step of the explicit flow solver. The method must be fast, as the grid is modified many times during the computation. In particular, it should lend itself to some degree of parallelism, and the method must not be memory (storage) intensive.

These constraints are met by 1) applying strict conservation on the discrete level and conducting the limiting process of FCT on the elements, 2) using classical h-enrichment/coarsening, as it does not require a major storage overhead and, due to its simplicity, lends itself easily to vectorization, 3) allowing only one level of refinement/coarsening per mesh change to minimize the logic, and thus the CPU requirements, and 4) avoiding successive subdivision of a triangle into two.

Grid Logic

When constructing the algorithm to refine or coarsen the grid, one faces the usual decision of speed vs storage. The more information from the previous grid is stored, the faster the new grid may be constructed. As storage requirement minimization was one of the goals of the present research, we tried to keep only the essential information needed between mesh changes without sacrificing an excessive amount of CPU time. In the present case, six integer locations per element are kept to identify the parent and son elements of any element.

The first three integers store the new three neighbor elements (sons) of an element that has been subdivided into four (the center element of the four is kept as parent). If the element has been subdivided into two elements, the neighbor element is stored in the first integer, whereas the remaining second and third integer locations for this element are set to zero.

The element from which the present element originated (the parent element) is stored in the fourth integer. If the parent element has been subdivided into two, the negative parent element number is stored, allowing the distinction between the 1:2 and 1:4 refinement cases.

The fifth integer denotes the local side of the parent element from which this element came.

Finally, in the sixth integer location the refinement level is remembered. These six integer locations per element are sufficient to construct further refinements or to reconstruct the original grid.

Error Indicator

Many possible error indicators have been suggested in the literature.[15–19,23–25] Numerical experience indicates that all perform similarly. However, the following requirements must be met for the present application: the error indicator must be fast. The error indicator should be dimensionless, so that more than one key-variable[19] can be monitored simultaneously. To be applicable to a large class of problems, the error estimator should be bounded (independent of the solution), so that preset refinement/coarsening tolerances can be employed. As the feature may move only very slowly or come to a standstill (e.g., a shock entering a very dense region), the error indicator must also be reliable for steady-state applications. Finally, the error indicator should mark for refinement not only regions with strong shocks, but also regions of weak shocks, contact discontinuities, and other weak features in the flow.

A classic interpolation estimate[19] used for steady-state computations[20–22] has been modified to meet these requirements. These estimators make use of an appropriate seminorm for the detection of those regions needing further refinement or coarsening, e.g., the H2-seminorm[16,20–22,24,25]

$$\|u - u^h\|_0 \le c \cdot h^2 \cdot |u|_2 \tag{6}$$

where u denotes the exact and u^h the approximate solution, c is a mesh-size independent constant, h is the characteristic mesh size, and

$$|u|_2 = \sqrt{\int_\Omega \sum_{i,j} \left[\frac{\partial^2 u}{\partial x^i \partial x^j}\right]^2} \tag{7}$$

Second derivatives are justified here because the shape functions used in the finite-element discretization are linear. Numerically, the second derivatives at the nodes are evaluated first via a variational statement and the integral (7) is approximated conservatively by evaluating the maximum second derivative at the associated nodes for each element. For linear elements of constant length h in one-dimensional, one obtains for the first step at the nodes:

$$e_I = h^{-2} \cdot |U_{I+1} - 2 \cdot U_I + U_{I-1}| \tag{8}$$

This error indicator is dimensional, and thus is not bounded a priori. A major defect noted in numerical experiments was that this error indicator tends to favor strong shocks. This results from the fact that second derivatives of a key variable u were utilized. Since the objective of the present study is to develop a methodology that accurately simulates weak shocks and contact discontinuities, the interpolation theory error indicator given by Eq. (8) was modified as follows:

$$E_I = \frac{|U_{I+1} - 2 \cdot U_I + U_{I-1}|}{|U_{I+1} - U_I| + |U_I - U_{I-1}| + \theta} \tag{9}$$

where

$$\theta = \epsilon \left[|U_{I+1}| + 2 \cdot |U_I| + |U_{I-1}| \right]$$

Dividing the second derivatives by the absolute value of the first derivatives yields an error indicator that is bounded ($0 \le E_I < 1$), dimensionless, and prevents the eating up effect of strong shocks. In addition, the nondimensional error indicator permits the use of several critical parameters simultaneously. Thus, it is possible to use both density and vorticity for problems requiring the simultaneous tracking of shocks and vortices. The terms following ϵ in Eq. (9) are added as a noise filter in order not to refine wiggles or ripples that appear due to loss of monotonicity. The value for ϵ thus depends on the algorithm chosen to solve the PDEs that model the physical process investigated. The multidimensional form of this error indicator is given by

$$E^I = \sqrt{\frac{\sum_{k,l} \left(\int_\Omega N^I_{,k} N^J_{,l} \, d\Omega \cdot U_j \right)^2}{\sum_{k,l} \left(\int_\Omega \left[|N^I_{,k}| |N^J_{,l} U_j| + \epsilon \left(|N^J_{,l}| |U_j| \right) \right] d\Omega \right)^2}} \tag{10}$$

where N^I denotes the shape-function of node I.

After the values of the error indicators in the elements are determined, all elements lying above a preset threshold value are refined, while all elements lying below a preset threshold value are coarsened.

Results

The transient, two-dimensional, finite-element shock-capturing scheme on unstructured grids described previously was applied in

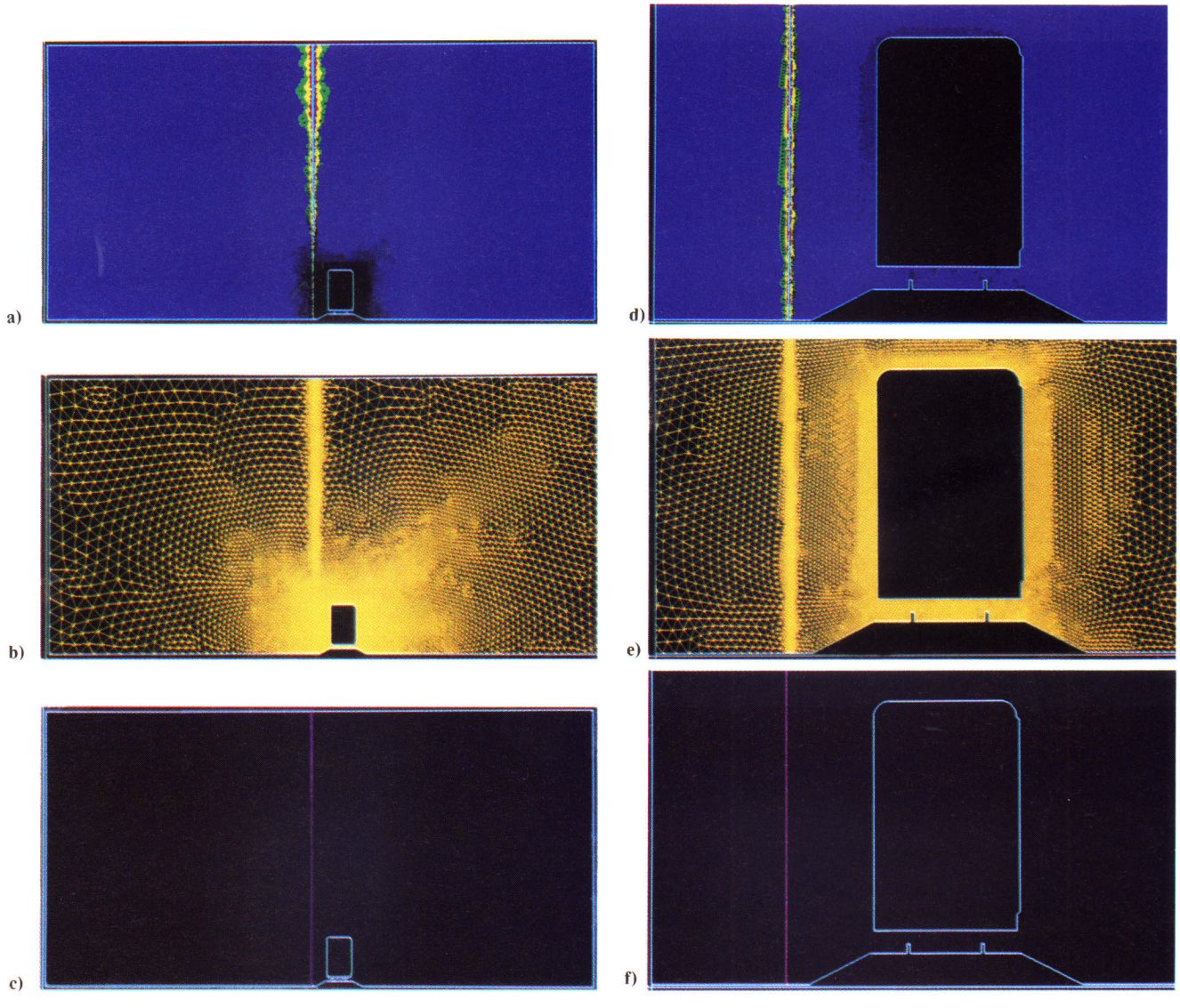

Fig. 1 Initial mesh refinement levels, computational grid and pressure contours for the complete computational domain (Figs. 1a–1c) and for an expanded zone near the box (Figs. 1d–1f).

this research effort to the study of a shock interacting with a box suspended above a rigid elevated surface. The area between the box and the surface was partially blocked by the box support beams.

Figures 1–11 show combinations of computational mesh, grid refinement levels, pressure, density, vorticity, and Mach number contours at several times. The grid was adapted every seven time steps. Density was chosen as the key variable for the error indicator. The incident weak shock travels from left to right, with a shock Mach number of 1.3. The color contour plots presented used 256 contours, with blue representing the lowest value and magenta the highest. With respect to the mesh refinement procedure, one level of mesh refinement is defined as the division of a triangle into four parts, performed by connecting the midfaces. The color designations for the mesh refinement levels are blue for the original grid, and green, yellow, red, magenta, and cyan for one, two, three, four, and five refinement levels, respectively. Two parameters control mesh refinement: the maximum number of refinement levels desired (five levels for this example), and the minimum normal height allowed below which the grid may not be further refined. Thus, near the box where the original grid has fine resolution, only two or three refinement levels were obtained. Conversely, five refinement levels will be obtained at zones of coarse initial grid, such as far above the box.

The results demonstrate that all shocks developed in the computational domain are captured as sharp discontinuities, validating the effectiveness of the scheme used. The results at $t = 6$ (all times are nondimensional) demonstrate the advantage of using an adaptive scheme, as the shocks were sharply captured even after propagating very large distances. Achieving similar shock resolution with a fixed-mesh methodology would have required maintaining a fine grid virtually everywhere in the computational domain, at a significantly (perhaps prohibitively) higher computational cost. Grid refinement is observed as the shocks propagate into new areas, while grid coarsening is observed in areas already traversed by the shocks. It should be noted that the solution obtained above the box at later times indicates a compression wave rather than a shock. This is the correct physical solution as the initial reflected shock above the box (Fig. 6a at $t = 1.2$ and Fig. 9a at $t = 2.6$) was significantly weakened by the strong expansion over the box. Results obtained in other simulations using significantly stronger shocks demonstrated a reflected shock above the box, even at very late times.

Figure 1 shows the mesh, mesh refinement levels, and pressure contours for the complete computational domain and for an expanded view around the box at $t = 0$. A highly refined mesh was

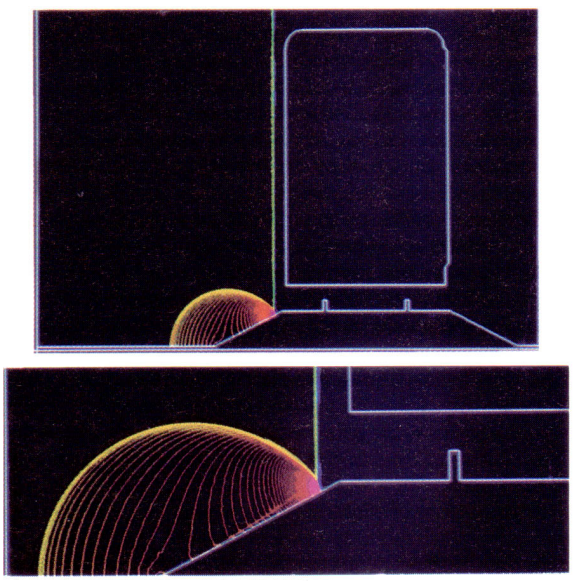

Fig. 2 Expanded views of pressure and density contours around the box, $t = 0.4$.

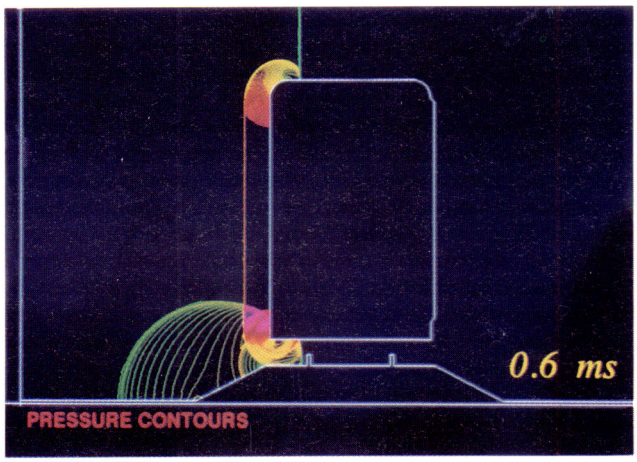

Fig. 3 Expanded view of pressure contours around the box, $t = 0.6$.

obtained only in the immediate vicinity of the shock. These figures indicate the futility of any attempt to grid such a computational domain, which is several hundred meters in each direction, with a uniform fine resolution grid that will yield captured shock wave thickness of less than 0.6 cm (about the average shock thickness obtained in this computation).

A regular Mach reflection from the ramp is observed at $t = 0.4$ (Figs. 2). The well-resolved slip line (shown in the density data, Fig. 2b) demonstrates one of the advantages of employing density rather than pressure as the critical refinement parameter. A comparison of the predicted pressure values behind the Mach stem with available experimental data showed very good agreement. The incident shock hits the box at $t = 0.46$.

The solution around the complete box at $t = 0.6$ (Fig. 3) shows a curved shock reflection from the top-upstream corner of the box, followed closely by an expansion fan. An expanded view of pressure contours near the bottom of the box at $t = 0.5$ (Fig. 4a) shows the nonperturbed incident shock (shock 1*a*), the main shock reflection from the upstream surface of the box (shock 1), the rarefaction waves expanded from the upstream-bottom corner of the box (wave 5) and the upstream top corner of the elevation (wave 4) after the main shock passage, the reflected ramp shock (shock 2), and the curved Mach stem (shock 3) that was further weakened by the interaction with the rarefaction wave 4. The expanded view under the box at $t = 0.6$ (Fig. 4b), shows the primary reflected shock from the box (shock 1), its reflection from the top of the elevation (shock 1a), the rarefaction wave centered at the upstream bottom corner of the box (wave 5); the reflected ramp shock (shock 2), its reflection from the box (shock 2*a*), and the rarefaction wave produced upon the impact of this wave on the box's upstream bottom corner (wave 2*b*), the incident Mach stem under the box (shock 3); and the expansion wave (wave 4) centered at the upstream corner of the ramp.

A comparison of the adapted mesh and mesh refinement levels at $t = 0.8$ (Figs. 5a and 5b) with the pressure results (Fig. 5c) demonstrates the ability of the grid adaptation routine to adapt to all density gradients. Due to the initially finer grid under the box, only three refinement levels were obtained there. In contrast, five refinement levels were observed away from the box, where the initial grid was fairly coarse. The pressure results at this time indicate that the shock diffraction over the top upstream curved corner of the box produced a triple point connecting the incident shock, a Mach stem, and a curved reflected shock (Fig. 5c). Ramp shock reflection (shock 2 in Fig. 4b) from the front surface of the box formed a high-amplitude Mach stem traversing the front surface of the box.

Complex flow processes were observed under the box. Examination of the expanded views under the box at $t = 0.7$ (Fig. 4c) and $t = 0.8$ (Fig. 4d) shows many interesting shock diffraction processes. At $t = 0.7$, the incident Mach stem has just cleared the up-

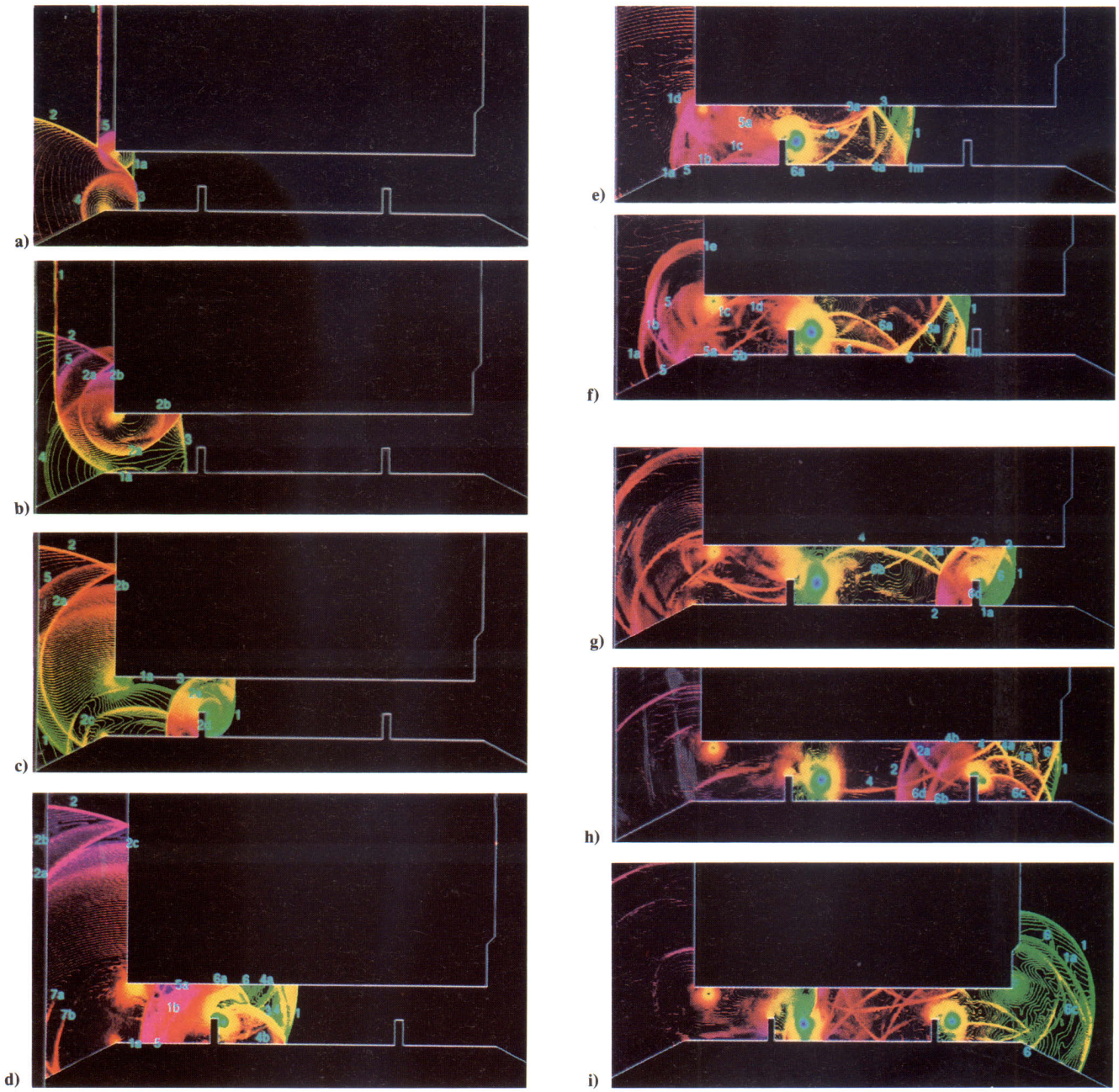

Fig. 4 Expanded views of pressure contours between the bottom of the box and the top of the elevation: a) $t = 0.5$, b) $t = 0.6$, c) $t = 0.7$, d) $t = 0.8$, e) $t = 0.9$, f) $t = 1.0$, g) $t = 1.1$, h) $t = 1.2$, and i) $t = 1.4$.

stream support beam (shock 1). The reflection of the incident shock from the beam has propagated upstream (shock 3 at $t = 0.7$ and shock 1*a* at $t = 0.8$) and, due to its curvature, partially reflected from the bottom of the box (shock 1*b* at $t = 0.8$). The diffracted incident Mach stem (shock 1) downstream of the beam has impacted on the top of the elevation at $t = 0.7$, and was reflected as shock 3 at $t = 0.8$. Immediately behind it, and partially merged, is shock 2*d*, which is the transmitted part (across the beam) of shock 2*a* at $t = 0.6$. The ramp shock and its reflection from the box (shocks 2 and 2*a* in Fig. 4b) are now shocks 2 and 2*a*; the expanding rarefaction waves 2*b* and 5 at $t = 0.6$ (Fig. 4b) are waves 2*b* and 5 at $t = 0.7$, and waves 2*c* and 2*b*, respectively, at $t = 0.8$; the reflection of the main shock (shock 1 in Fig. 4b) from the top of the elevation is shock 1*a* at $t = 0.7$, and 7*a* at $t = 0.8$, while the reflection of shock 2*a* at $t = 0.6$ (which is the reflection of the reflected ramp shock from the box) is shock 2*c* at $t = 0.7$, and shock 7*b* at $t = 0.8$. The evolution of these shocks is important in determining the vibrations on the box. Shock 1*a* at $t = 0.7$ has partially reflected from the upstream beam (shock 5 at $t = 0.8$, which has also reflected from the bottom of the box as shock 5*a*), and partially transmitted as shock 4 at $t = 0.8$, which has reflected from both the bottom of the box (shock 4*a*) and the top of the elevation (shock 4*b*). Similarly, shock 2*c* has expanded up- and downstream (shock 6), and reflected from the bottom of the box (shock 6*a*). The low-pressure zone near the top of the beam indicates a high-velocity zone created as a result of flow acceleration around the top of the beam and the attached vortex sheet, which has just begun its roll-up process.

While the incident shock continued propagating above the box, the triple point height grew linearly with time, and the circular expansion waves from both the bottom and top upstream corners also continued growing linearly with time (Figs. 3, 5c, 6a, and 7c), the most interesting shock evolution processes occurred under the box. Examination of the pressure contour results under the box at $t = 0.9$ (Fig. 4e) and $t = 1.0$ (Fig. 4f) shows the virtual separation of the shock system between the support beams and the reflected shocks upstream of the beams. This separation results from the

growing vortex near the upstream support beam, which will accelerate and break any approaching shock. At $t = 0.9$, the leading shock (shock 1) has been completely merged with shock 4 at $t = 0.8$. Meanwhile, we observe the formation and rise of the triple point between shocks 1 and 3, and Mach stem 1m. Shock 3 at $t = 0.9$ was formed by the merging of shocks 3 and 4*b* at $t = 0.8$, an almost completed merger as two shocks are observed to reflect from the bottom of the box at $t = 0.9$ (shocks 3*a* and 4*b*). Nevertheless, a single reflected shock is observed after the shocks were reflected again from the top of the elevation ($t = 1.0$). Another shock system observed between the support beams are shock 6 (at $t = 0.9$), which evolved from shock 6*a* at $t = 0.8$, and its reflection from the top of the elevation, shock 6*a*.

Shock wave reflection upstream is characterized both by shock wave reverberation between the bottom of the box and the top of the elevation and shock interaction with the vortex emanating from the upstream bottom corner of the box. As an example of the first phenomenon, we point to shock 1*b* at $t = 0.8$ (which has just reflected from the bottom of the box), propagating down, and reflecting from the top of the elevation as shock 1*c* ($t = 0.9$), and reflecting again from the bottom of the box as shock 1*d* ($t = 1.0$). Similar reflection pattern was observed for shock 5*a*.

Typical shock-vortex interaction can be observed in Figs. 4d and 4f ($t = 0.8$ and 1.0, respectively). The reflection of the curved shock 1*a* from the bottom of the box (shock 1*b* at $t = 0.8$), resulted in the formation of a triple point, with increased height from the surface. At $t = 0.82$, the Mach stem near the surface and the two shocks (shock 1*a* and 1*b*) interact with the vortex attached to the upstream bottom corner of the box. The result is an acceleration and diffusion of the shock near the surface of the box; both effects decrease with increased distance from the surface. These processes result in the upstream acceleration and diffusion of compression

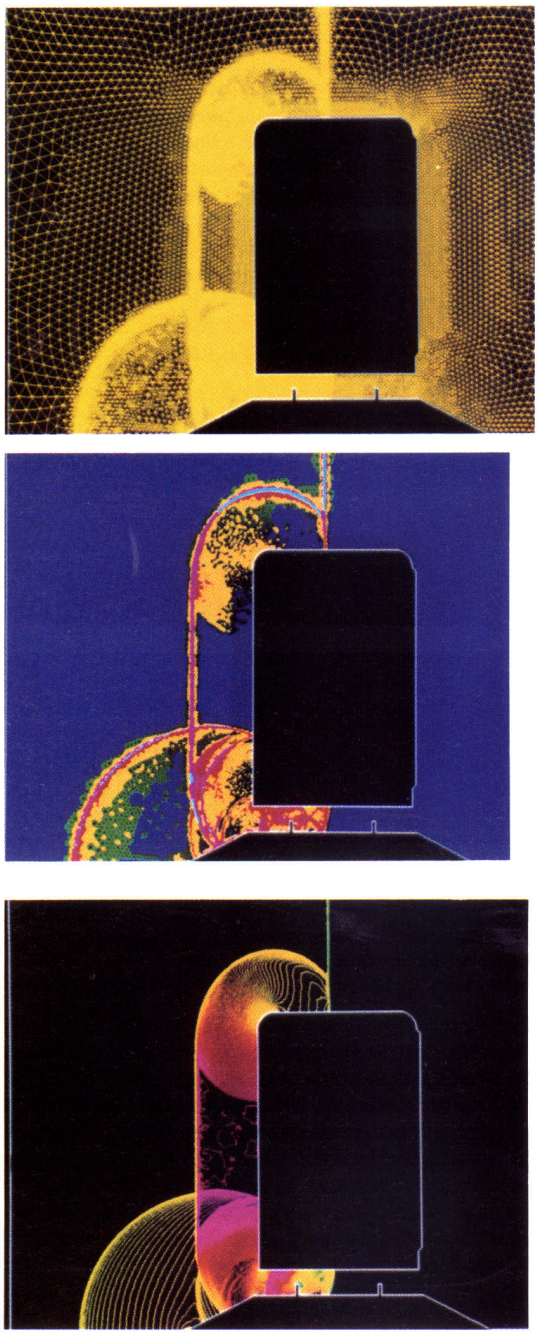

Fig. 5 Expanded views of computational grid, mesh refinement levels, and pressure contours around the box, $t = 0.8$.

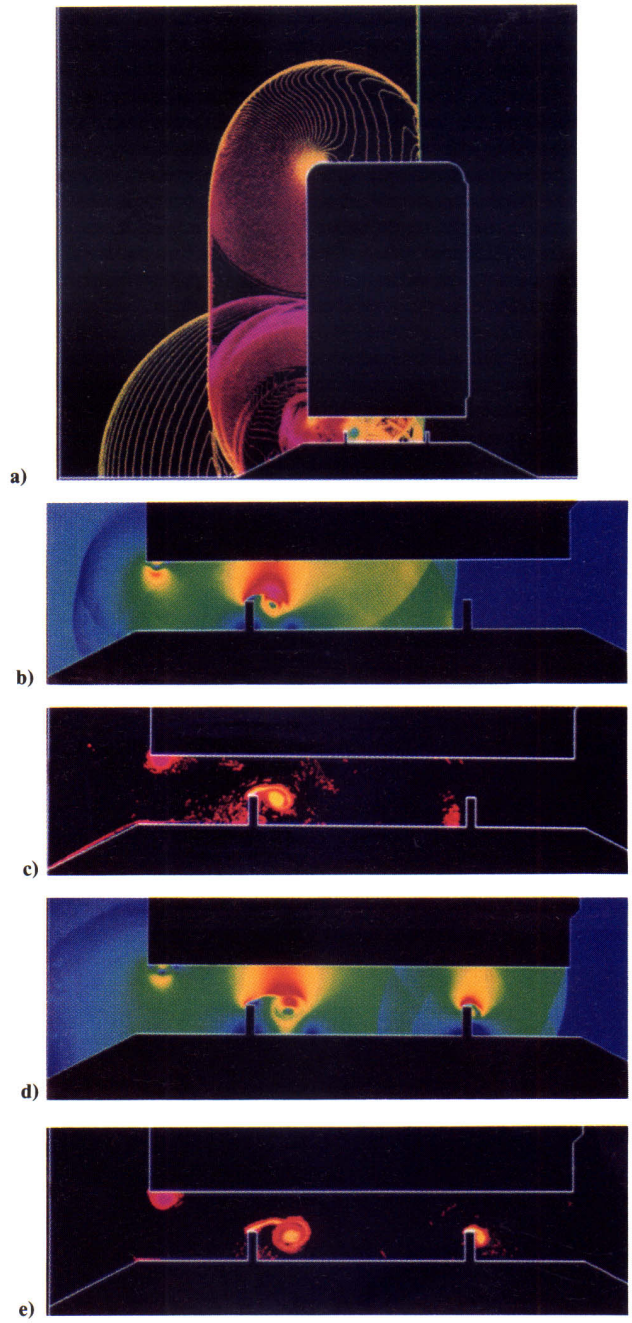

Fig. 6 Expanded views of pressure (Fig. 6a), Mach number (Fig. 6b) and vorticity contours (Fig. 6c) around the box at $t = 1.0$, and Mach number (Fig. 6d) and vorticity contours (Fig. 6e) at $t = 1.2$.

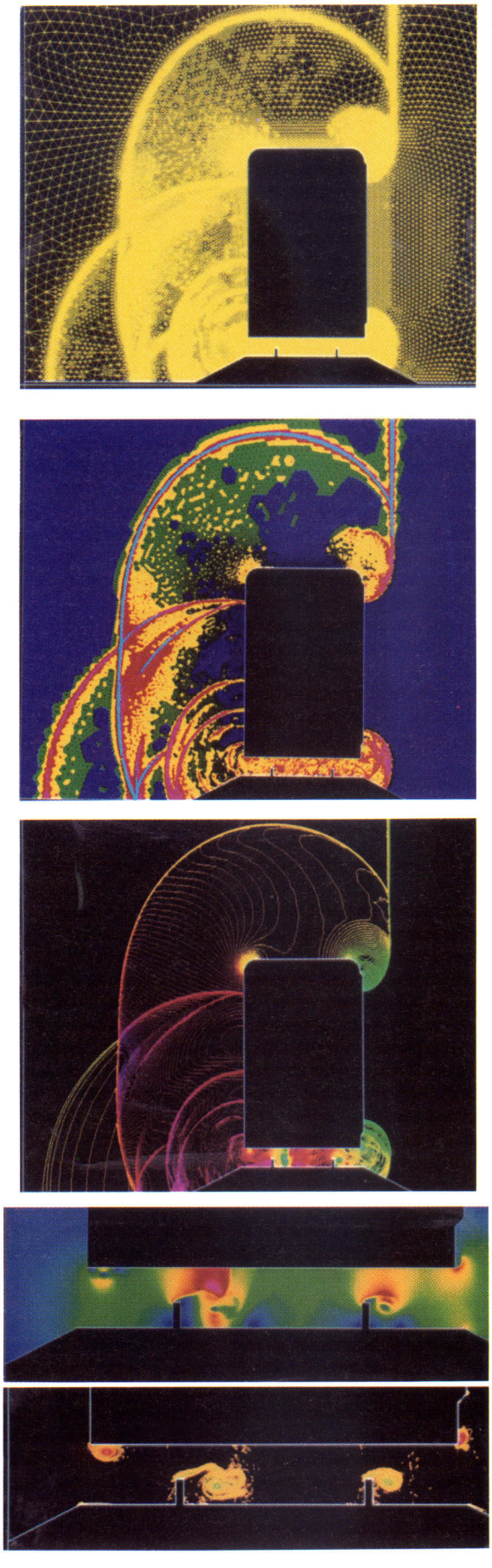

Fig. 7 Expanded views of computational grid (Fig. 7a), mesh refinement levels (Fig. 7b), pressure (Fig. 7c), Mach number (Fig. 7d) and vorticity contours (Fig. 7e) around the box, $t = 1.4$.

wave 1*d* between $t = 0.8$ and $t = 1.0$. The next shock wave system, shocks 5 and 5*a*, experience similar though weaker processes, perhaps due to the weakening of the vortex.

At $t = 1.0$ (Fig. 4f), the reflected ramp shock (shock 4a at $t = 0.9$) and the incident Mach stem (shock 1) were about to merge; we also observe its the reflection from the top of the elevation; shock 3 is the reflected shock 3 at $t = 0.8$, while its reflection from the bottom of the box and the subsequent reflection from the top of the elevation are shocks 3*a* and 4; shock 6*a* is the reflection of shock 6 at $t = 0.9$ from the top of the elevation. Numerous shocks were observed at this time to reflect upstream. Prominent among them are the evolutions of shocks 2, 2*a* and 5 at $t = 0.8$, and the system of shocks created by the reverberation of these curved shocks between the bottom of the box and the top of the elevation.

The very-low-pressure zone near the upstream support beam indicates the rapid roll-up of a vortex sheet anchored at the top-upstream corner of the beam (Fig. 5c and Figs. 4e–4i). The vortex roll-up process was enhanced by vortex interaction with the system of curved reflected shocks reverberating between the bottom of the box and the top of the elevation. A much weaker vortex sheet has also been formed near the upstream bottom corner of the box. Mach number results at $t = 0.8$ and later (Figs. 6b and 6d, at $t = 1.0$ and $t = 1.2$, respectively), demonstrate strong flow acceleration due to the vortex roll-up and the reduction of the effective flow area between the top of the elevation and the bottom of the box, with the highest velocities above the inner-most vortex.

Since vortex dynamics is a phenomenon normally associated with viscous flow processes, while the present numerical scheme only solves the Euler equations, the source of this vorticity deserves further discussion.

Vorticity production, as modeled in the Bjerknes Theorem,[26] incorporates both viscous and inviscid contributions, and is expressed as:

$$\frac{D\vec{\xi}}{Dt} = -\nabla\left(\frac{1}{\rho}\right) \times \nabla P + \nu\nabla^2\vec{\xi} \tag{11}$$

where $\vec{\xi}$ = vorticity, ν = kinematic viscosity, p = pressure, and ρ = density.

A time-scale and order-of-magnitude analysis of these terms indicates that the current vorticity production is controlled by the baroclinic effect (i.e., the first term in the equation, which represents the nonalignment of pressure and density gradients), and thus can be predicted by the inviscid code. Laser-schilieren shadowgraph data were produced in a similar shock-box interaction experiment. This experiment was conducted using a subscale model in a shock tube facility and demonstrated vortex sheet rollup within a few microseconds after the shock diffracted around the corner, a time period too short for viscous processes to significantly affect the flow. The numerical predictions for this experiment were in excellent agreement with the experimental data. Due to lack of space they will be presented in a future publication.

The incident shock propagated past the downstream support beam at $t = 1.03$. Results at $t = 1.1$ and $t = 1.2$ (Figs. 4g and 4h, respectively) show that similar to the shock diffraction process over the upstream beam (Fig. 4d at $t = 0.8$), incident shock diffraction around the downstream beam resulted in the formation of curved diffracted and reflected shocks; shocks 1 and 1*a* are the transmitted shock wave and its reflection from the top of the elevation, respectively, while shocks 2 and 2*a* are the reflected shock and its reflection from the bottom of the box. The merged shock formed of shocks 3*a* and 6 (at $t = 1.0$) has been partially transmitted as shock 6 ($t = 1.1$) and was later reflected from the top of the elevation as shock 6*c* ($t = 1.2$), and partially reflected from the beam as shock 6*d* (at $t = 1.1$ and $t = 1.2$). Shocks 4 and 6*a* at $t = 1.0$ continued to reverberate and produce shocks 4, 6*a*, and 6*b* at $t = 1.1$, and shocks 4, 4*a* and 4*b* (beam reflection), and 6*b* at $t = 1.2$. The vorticity contour plots, Figs. 6c and 6e, at $t = 1.0$ and $t = 1.2$, respectively, indicate significant enhancement of the rolled-up vortex sheet behind the upstream beam. This is due to the interaction with the family of curved reflected shocks, and the initiation of a vortex sheet behind the downstream beam.

The successful continued grid adaptation is demonstrated again at $t = 1.4$. A comparison of the computational grid (Fig. 7a), grid refinement level (Fig. 7b), and pressure, Mach number, and vorticity contours (Figs. 7c, 7d and, 7e, respectively) demonstrate the ability of the new methodology to adapt to both strong and weak density gradients.

The shocks that propagated under the box emerged at $t = 1.22$. The higher stagnation pressure under the box resulted in faster propagation speed than above, and thus the incident shock propagating below emerged a short time earlier. Pressure results at $t = 1.4$ (Fig. 4i) indicate that four primary shocks emerged: the incident shock (shock 1), its reflection from the top of the elevation (shock 1*a*), shock 6*c*, and shock 6, which has been weakened by its upward expansion and broken due to its interaction with the stronger shocks 1*a* and 6*c*. The expansion of these shocks around the bottom downstream corner of the box and the corner of the elevation resulted in the immediate formation of a counter-clockwise rotating vortex sheet anchored at the corner and a cylindrical expansion wave. The bottom-produced rarefaction could not propagate upstream beyond the downstream beam, due to the transonic flow between the beam and the bottom of the box.

Among the upstream reflected shocks observed are the primary reflection from the box upstream surface, reflections of the Mach stem from the box, and several shock reflections from the upstream support beam. The system of shocks between the beams continued reverberating and producing new shocks. The interactions between these curved shocks with the rolled-up vortex attached to the upstream beam resulted in the breakup of this sheet, as observed at $t = 1.4$ (Fig. 7e) and $t = 1.6$ (Fig. 8a).

Figure 8 shows vorticity contours at several times. While vorticity production was fairly low for shock diffraction over the rounded upper downstream corner of the box, the system of shock waves reverberating between the support beams and between the top of the elevation and the bottom of the box both enhanced and broke up the rolled-up vortices attached to the support beams, as shown in Figs. 8a, 8b, 8c, 8d, and 8e at $t = 1.6$, 1.8, 2.0, 2.2, and 2.4, respectively. Meanwhile, the vortices attached to the bottom corners of the box continued their rollup process; the one attached to the downstream corner rolled up about four times at $t = 2.4$ (Fig. 8e).

The shocks diffracting around the downstream side of the box interacted with the opposite corners at $t = 2.6$. The computational grid, the grid adaptation levels, and the pressure and Mach number contour results at $t = 2.4$ (Figs. 9a–9d) demonstrate the excellent shock adaptation capabilities of the developed methodology, even after propagating long distances. The large disparity between the long shock propagation distance and the small size of the resolved vortices or the captured shock thickness clearly demonstrates the economical advantage of applying an adaptive refinement/coarsening scheme as compared to a fixed-mesh scheme.

The shock that has diffracted over the top interacted at $t = 2.6$ with the vortex sheet anchored at the bottom downstream corner (Fig. 8f). Since this curved diffracted shock carried vorticity of the opposite sign and of about equal magnitude to the vorticity of the attached vortex sheet, the interaction caused the eventual detachment of the vortex sheet from the corner and its downstream convection. Flow area constriction due to the vortices shed from both the upstream and downstream beams (Fig. 7d and 9d) resulted in flow acceleration to supersonic velocities, specifically, downstream of the downstream beam ($M = 1.28$). The instantaneous local flow area expansion near the downstream bottom corner of the box resulted in the formation of an oblique shock wave and a deceleration to $M = 0.65$.

The downward-propagating shock downstream of the box hit the bottom bevel at $t = 3.1$ and reflected upward. Meanwhile, the shock that emerged from under the box continued its downstream-

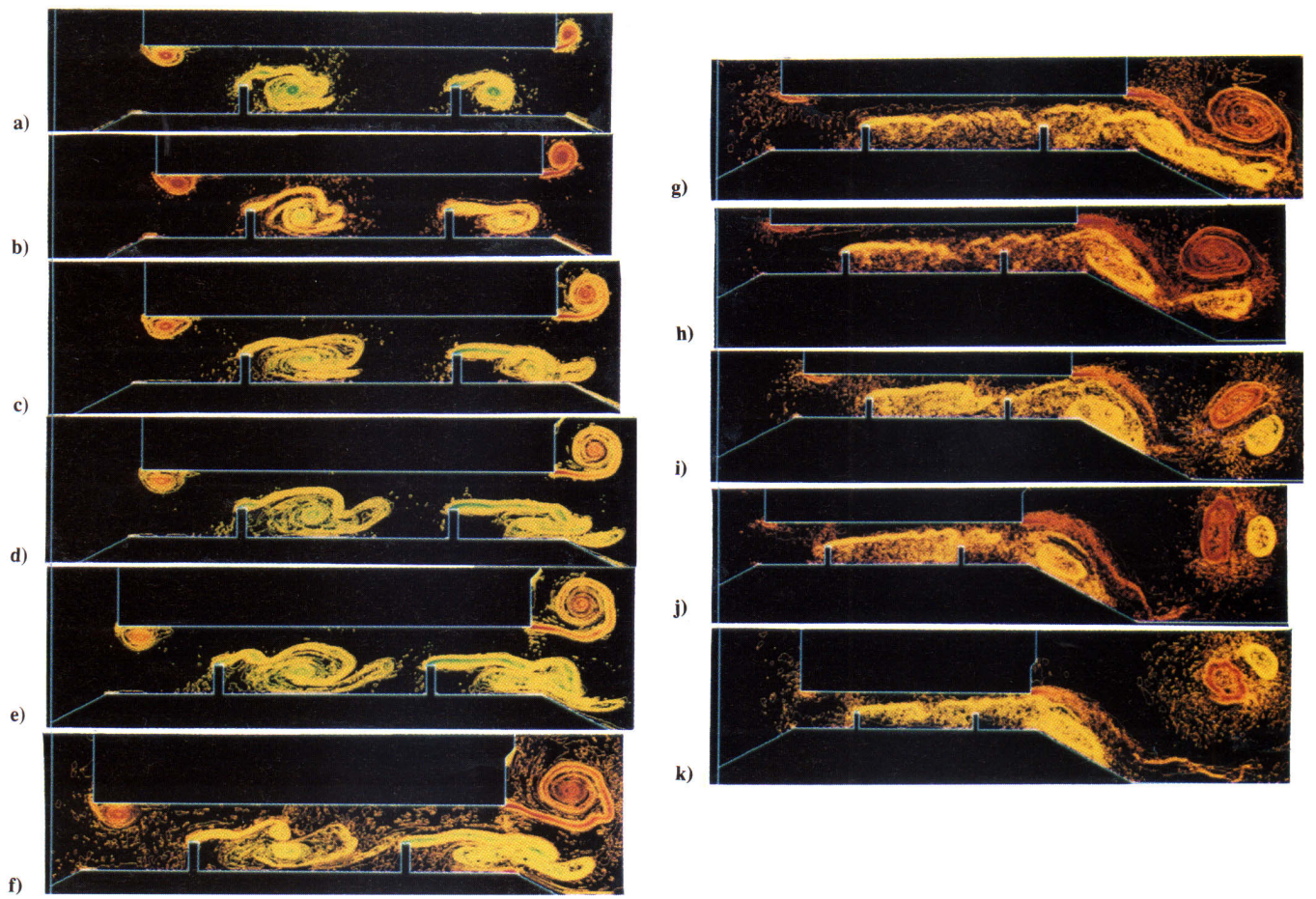

Fig. 8 Expanded views of vorticity contours between the bottom of the box and the top of the elevation: a) $t = 1.6$, b) $t = 1.8$, c) $t = 2.0$, d) $t = 2.2$, e) $t = 2.4$; f) $t = 2.6$, g) $t = 3.2$, h) $t = 3.6$, i) $t = 4.2$, j) $t = 5.0$ and k) $t = 6.0$.

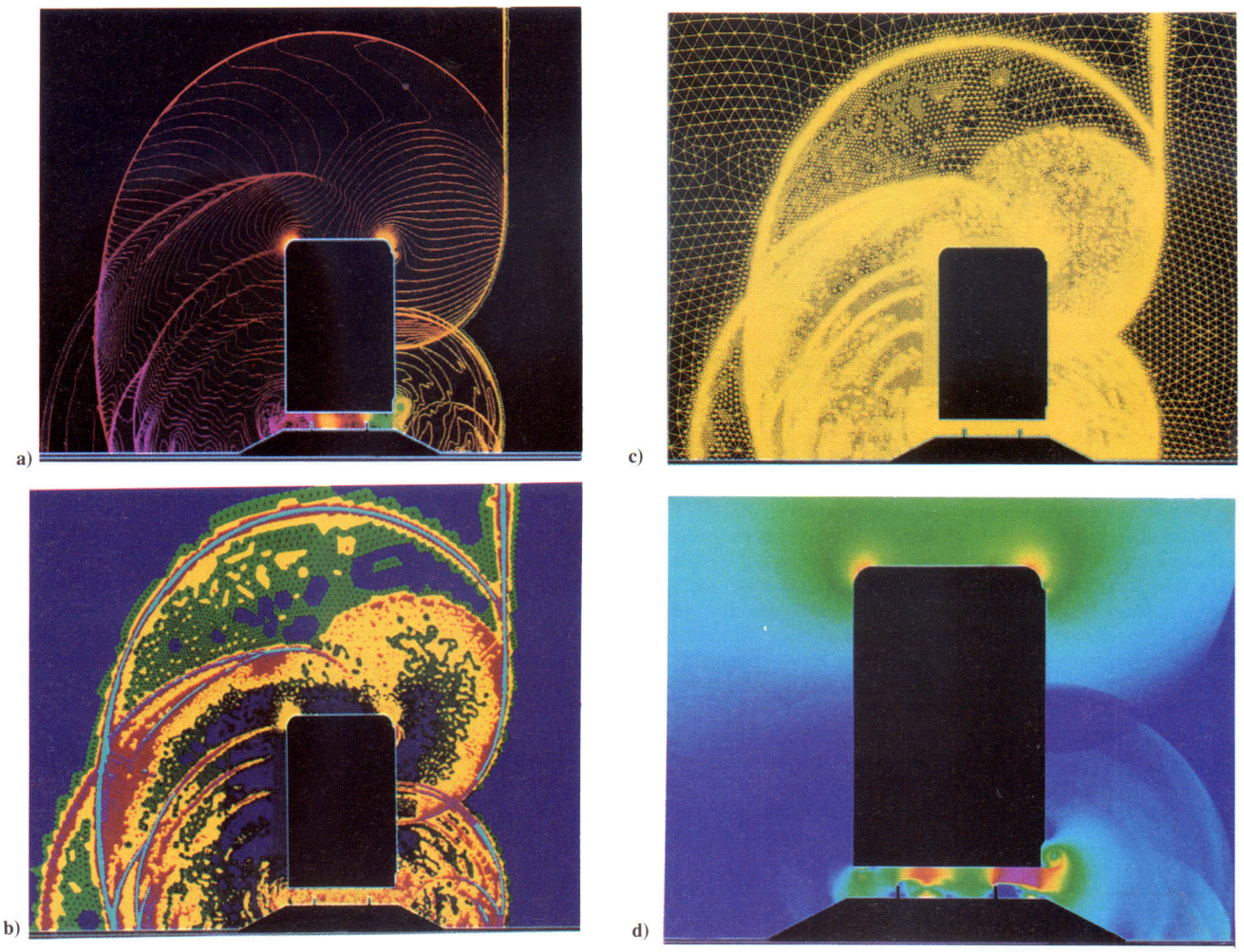

Fig. 9 Expanded views of computational grid (Fig. 9a), mesh refinement levels (Fig. 9b), and pressure (Fig. 9c) and Mach number contours (Fig. 9d) around the box, $t = 2.4$.

and-up propagation, though shock propagation upward was inhibited by the transonic flow above the box. This blockage effect temporarily trapped a relatively high pressure zone downstream of the box, which could not be relieved through the channel under the box due to the transonic flow in this zone. Meanwhile, the vortices shed from the downstream beam and bottom corner were convected downstream by the flow, as shown in Figs. 8g, 8h, 8i, 8j, and 8k, at $t = 3.2$, 3.6, 4.2, 5.0, and 6.0, respectively. These results also show the breakup of the vortex sheet attached to downstream beam, the roll-up of the broken sheet into a weak, clockwise-rotating vortex (Fig. 8h), and the rolling of the pair of counter-rotating vortices by the flow (Figs. 8i–8k).

The computation was continued to $t = 8.0$, long after the system of shocks cleared the box. At this time the flow above the box was still transonic after reaching a maximum Mach number of $M = 1.35$ at $t = 4.5$. Thus, the upward propagation of the shock reflected from the downstream bevel was delayed, and its influence was still felt on the top of the box at $t = 6.0$ (Fig. 10). All shocks had propagated very long distances, but were still captured as sharp, nonoscillatory discontinuities. The captured shocks' thickness had not changed over the past several thousand steps, as all shocks were still captured over two to three elements, whereas the element size around the shock had not changed due to the adaptive procedure. These results demonstrate, at least for the present application, the advantage of adaptive-mesh schemes over fixed-grid schemes. Achieving similar shock resolution with a fixed-mesh methodology would have required maintaining a fine grid virtually everywhere in the computational domain, at a significantly (perhaps prohibitively) higher computational cost. Grid refinement was observed as the shocks propagated into new areas, while grid coarsening was observed in areas already traversed by the shocks. Finally, it should be noted that the solution obtained above the box at later times indicates a compression wave rather than a shock. This is the correct physical solution as the initial reflected shock above the box (Fig. 5c at $t = 0.8$ and Fig. 7c at $t = 1.4$) was significantly weakened by the strong expansion over the box (Fig. 9c at $t = 2.4$). Results obtained in other simulations using significantly stronger shocks demonstrated a reflected shock above the box, even at very late times.

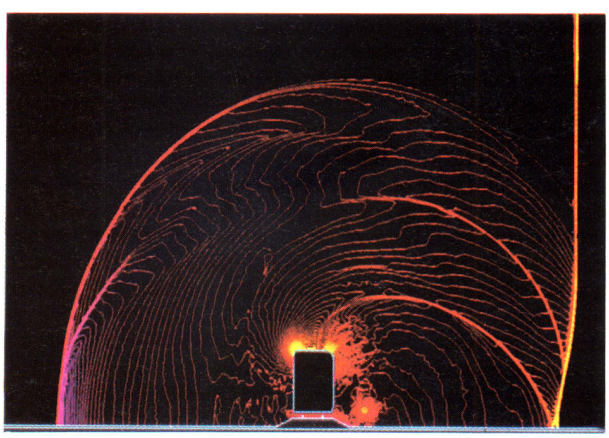

Fig. 10 Pressure contours around the box, $t = 6.0$.

Comparisons of experimental pressure and impulse time histories and the corresponding numerical predictions are shown in

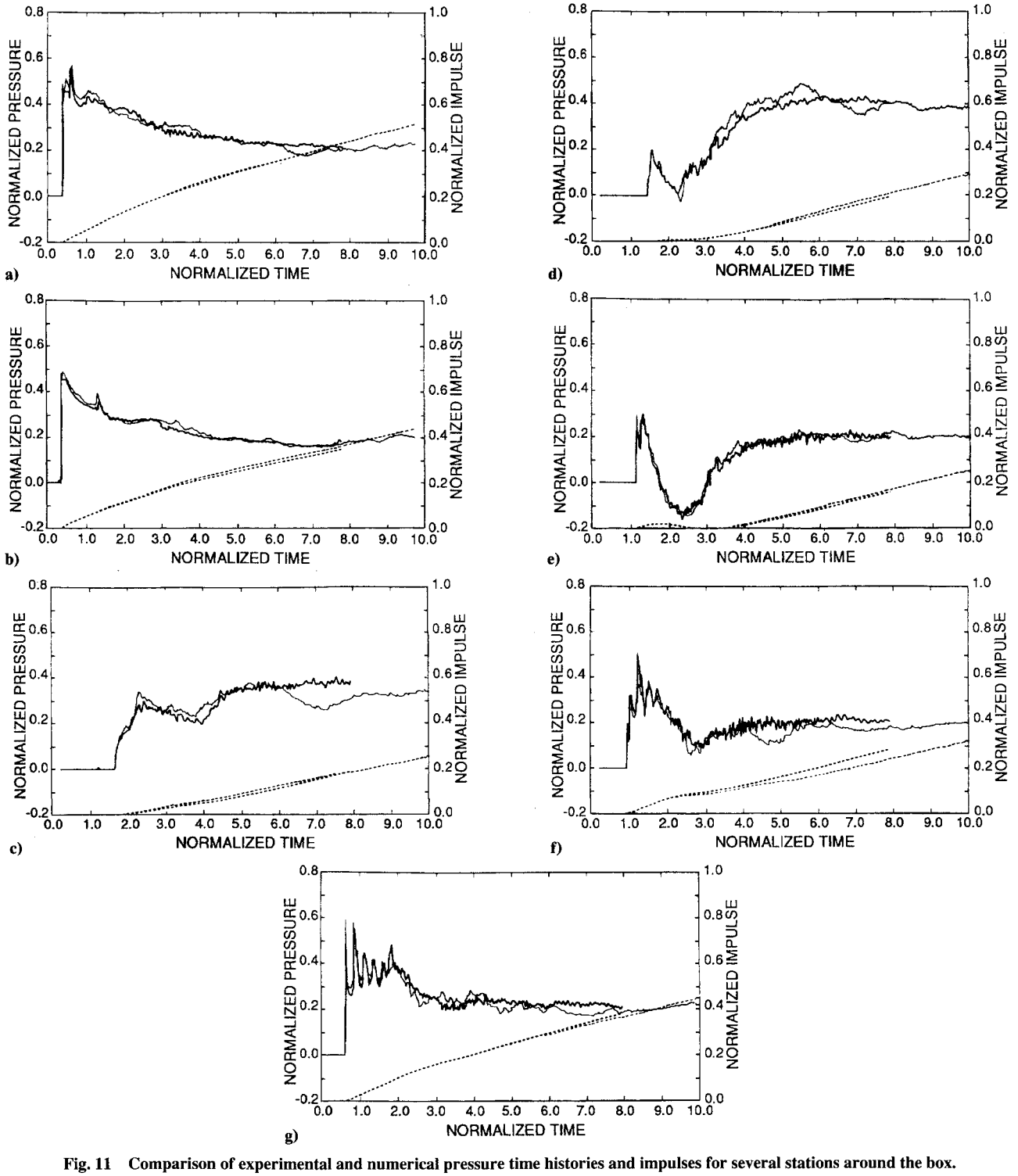

Fig. 11 Comparison of experimental and numerical pressure time histories and impulses for several stations around the box.

Figs. 11 at selected stations around the box. Stations *a* and *b* were located on the upstream surface of the box, station *c* on top, stations *d* and *e* on the downstream surface, and stations *f* and *g* on the bottom. The experimental data were obtained in a large shock tube facility. Since the experimental model spanned a significant portion of the width of the shock tube, it was appropriate to model this flow with a two-dimensional algorithm. The numerical pressure time histories and impulses (temporally integrated pressures) are shown as thicker lines to $t = 8.0$. The experimental pressure and impulse data are shown in thinner lines to $t = 10.0$. Very good agreement is demonstrated at all locations. Physical processes controlled by shock physics were predicted extremely well. For instance, very good agreement is demonstrated between the predicted and measured pressure-time histories at stations *f* and *y*, located under the box; these stations exhibit a multishock system that resulted from the repetitive shock reflection from the top of the elevation, the support beams, and the bottom of the box. In contrast, the late-time experimental data (well past the diffraction phase) for stations on the box top and back indicate periodic three-dimensional vortex shedding, a physical process that cannot be properly modeled by the present two-dimensional model.

A final note related to the computational performance of the code: computation time for approximately 6800 time steps consumed approximately six hours of CPU time on a Cray 2/8-128 computer (single processor). Computation time was approximately 60 μs per node per time step.

Summary and Conclusions

A new transient, two-dimensional, finite element shock-capturing scheme on unstructured grids was applied to the study of shock

interaction with a box suspended above a rigid, elevated surface. The area between the box and the surface was partially blocked by the box support beams, resulting in complex shock diffraction processes. The results demonstrate the ability of the new adaptive refinement/coarsening algorithm to resolve shocks in a sharp-nonoscillatory manner. In addition to interesting shock wave propagation and interaction processes, the results demonstrate the capability of the new code to capture, and define in great detail, vortices shed from sharp corners.

Among the more interesting shock propagation processes observed were a) shock diffraction around sharp corners and the immediate formation of vortices, no doubt due to the baroclinic effect; b) interaction of diffracted curved shocks with vortex sheets carrying vorticity of identical or opposite sign, resulting in either vortex enhancement or breakup; c) containment of the high-pressure zone (i.e., blockage of upward propagation of shocks) on the downstream side of the box by the supersonic/transonic flow above the box; and d) the blockage of the upstream propagation of the rarefaction wave in the channel under the box due to the transonic flow above the downstream support beam.

Acknowledgments

Funding for this research work was provided by the Defense Nuclear Agency. Paul J. Castleberry Jr. was the technical program monitor. Computer time was generously provided by Cray Research Inc., Eagan, MN, and Steve Perry of the Cray Research Inc. Eastern Region Office, Beltsville, MD.

References

[1]Woodward, P., and Colella, P., "The Numerical Simulation of Two-Dimensional Fluid Flow with Strong Shocks," *Journal of Computational Physics*, Vol. 54, 1984, pp. 115–173.

[2]Glaz, H. M., Colella, P., Glass, I. I., and Deschambault, R. L., "A Numerical Study of Oblique Shock-Wave Reflections with Experimental Comparisons," *Proceedings of the Royal Society of London A*, Vol. 398, 1985, pp. 117–140.

[3]Fry, M., Tittsworth, J., Kuhl, A., Book, D. L., Boris, J. P., and Picone, M., "Transport Algorithms with Adaptive Gridding," *Proceedings of the 13th International Symposium on Shock Tubes and Waves*, edited by C. E. Treanor and J. G. Hall, Springer-Verlag, Berlin, 1981, pp. 376–384.

[4]Roe, P. L., "Approximate Riemann Solvers, Parameter Vectors and Difference Schemes," *Journal of Computational Physics*, Vol. 43, 1981, pp. 357–372.

[5]Harten, A., "High Resolution Schemes for Hyperbolic Conservation Laws," *Journal of Computational Physics*, Vol. 49, 1983, pp. 357–393.

[6]Sweby, P. K., "High Resolution Schemes Using Flux Limiters for Hyperbolic Conservation Laws," *SIAM Journal of Numerical Analysis*, Vol. 21, 1984, pp. 995–1011.

[7]Berger, M. J., and Oliger, J., "Adaptive Mesh Refinement for Hyperbolic Partial Differential Equations," *Journal of Computational Physics*, Vol. 53, 1984, pp. 484–512.

[8]Zalesak, S. T., "Fully Multidimensional Flux-Corrected Transport Algorithm for Fluids," *Journal of Computational Physics*, Vol. 31, 1979, pp. 335–362.

[9]Boris, J. P., and Book, D. L., "Flux-corrected Transport. I. SHASTA, a Transport Algorithm that Works," *Journal of Computational Physics*, Vol. 11, 1973, p. 38.

[10]Boris, J. P., and Book, D. L., "Flux-corrected Transport. III. Minimal-Error FCT Algorithms," *Journal of Computational Physics*, Vol. 20, 1976, pp. 397–431.

[11]Paillere, H., and Powel, K., "A Wave-Model-Based Refinement Criterion for Adaptive-Grid Computation of Compressible Flows," AIAA Paper 92-0322, Jan. 1992.

[12]Parpia, I., and Michalek, D., "A Nearly Monotone Genuinely Multidimensional Scheme for the Euler Equations," AIAA Paper 92-0325, Jan. 1992.

[13]Parrott, A. K., and Christie, M. A., "FCT Applied to the 2-D Finite Element Solution of Tracer Transport by Single Phase Flow in a Porous Medium," *Proceedings of the ICFD-Conference on Numerical Methods in Fluid Dynamics*, Academic Press, New York, 1986.

[14]Löhner, R., Morgan, K., Vahdati, M., Boris, J. P., and Book, D. L., "FEM-FCT: Combining Unstructured Grids with High Resolution," *Communications on Applied Numerical Methods*, Vol. 4, 1988, pp. 717–730.

[15]Löhner, R., Morgan, K., Peraire, J., and Vahdati, M., "Finite Element Flux-Corrected Transport (FEM-FCT) for the Euler and Navier-Stokes Equations," *International Journal of Numerical Methods in Fluids*, Vol. 7, 1987, pp. 1093–1109.

[16]*Accuracy Estimates and Adaptive Refinements in Finite Element Computations*, edited by I. Babuska, J. Gago, E. R. de Arantes e Oliveira, and O. C. Zienkiewicz, Wiley, New York, 1986.

[17]Palmerio, B., and Dervieux, A., "Application of a FEM Moving Node Adaptive Method to Accurate Shock Capturing," *Proceedings of the First International Conference on Numerical Grid Generation in CFD* (Landshut, Germany), Pineridge, Swansea, Wales, UK, 1986, pp. 425–436.

[18]Schönauer, W., Raith, K., and Glotz, K., "The Principle of Difference Quotients as a Key to the Self-Adaptive Solution of Nonlinear Partial Differential Equations," *Computer Methods in Applied Mechanical Engineering*, Vol. 28, 1981, pp. 327–359.

[19]Dannenhoffer, J. F., and Baron, J. R., "Robust Grid Adaptation for Complex Transonic Flows," AIAA Paper 86-0495, Jan. 1986.

[20]Löhner, R., Morgan, K., and Zienkiewicz, O. C., "An Adaptive Finite Element Procedure for High Speed Flows," *Computer Methods in Applied Mechanical Engineering*, Vol. 51, 1985, pp. 441–465.

[21]Löhner, R., and Morgan, K., "Improved Adaptive Refinement Strategies for Finite Element Aerodynamic Computations," AIAA Paper 86-0499, Jan. 1986.

[22]Peraire, J., Vahdati, M., Morgan, K., and Zienkiewicz, O. C., "Adaptive Remeshing for Compressible Flow Computations," *Journal of Computational Physics*, Vol. 72, 1987, pp. 449–466.

[23]Smooke, M. D., and Koszykowsky, M. L., "Two-Dimensional Fully Adaptive Solutions of Solid-Solid Alloying Reactions," *Journal of Computational Physics*, Vol. 62, 1986, pp. 1–25.

[24]Oden, J. T., Devloo, P., and Strouboulis, T., "Adaptive Finite Element Methods for the Analysis of Inviscid Compressible Flow: I. Fast Refinement/Unrefinement and Moving Mesh Methods for Unstructured Meshes," *Computer Methods in Applied Mechanical Engineering*, Vol. 59, 1986, pp. 327–362.

[25]Löhner, R., "An Adaptive Finite Element Scheme for Transient Problems in CFD," *Computer Methods in Applied Mechanical Engineering*, Vol. 61, 1987, pp. 323–338.

[26]Bjerknes, V., Bjerknes, J., Bergeron, T., and Solberg, H., *Physikalische Hydrodynamik*, Springer-Verlag, Berlin, Germany, 1933.